Expert Systems With Applications 61 (2016) 1–15

Contents lists available at ScienceDirect

Expert Systems With Applications

journal homepage: www.elsevier.com/locate/eswa

Hessian based approaches for 3D lung nodule segmentation

L. Gonçalves [a], J. Novo [c,*], A. Campilho [a,b]

[a] INESC TEC - INESC Technology and Science. FEUP Campus, Dr. Roberto Frias 4200 - 465. Porto, Portugal
[b] Faculdade de Engenharia, Universidade do Porto. FEUP Campus, Dr. Roberto Frias 4200 - 465. Porto, Portugal
[c] University of A Coruña, Department of Computer Science. Campus de Elviña 15071. A Coruña, Spain

ARTICLE INFO

Article history:
Received 8 February 2016
Revised 6 April 2016
Accepted 13 May 2016
Available online 13 May 2016

Keywords:
Computer-aided diagnosis
Thoracic CT imaging
Lung cancer
Pulmonary nodule segmentation
Hessian-based approaches

ABSTRACT

In the design of computer-aided diagnosis systems for lung cancer diagnosis, an appropriate and accurate segmentation of the pulmonary nodules in computerized tomography (CT) is one of the most relevant and difficult tasks. An accurate segmentation is crucial for the posterior measurement of nodule characteristics and for lung cancer diagnosis.

This paper proposes different approaches that use Hessian-based strategies for lung nodule segmentation in chest CT scans. We propose a multiscale segmentation process that uses the central medialness adaptive principle, a Hessian-based strategy that was originally formulated for tubular extraction but it also provides good segmentation results in blob-like structures as is the case of lung nodules. We compared this proposal with a well established Hessian-based strategy that calculates the Shape Index (SI) and Curvedness (CV). We adapted the SI and CV approach for multiscale nodule segmentation. Moreover, we propose the combination of both strategies by combining the results, in order to take benefit of the advantages of both strategies.

Different cases with pulmonary nodules from the Lung Image Database Consortium and Image Database Resource Initiative (LIDC-IDRI) database were taken and used to analyze and validate the approaches. The chest CT images present a large variability in nodule characteristics and image conditions. Our proposals provide an accurate lung nodule segmentation, similar to radiologists performance. Our Hessian-based approaches were validated with 569 solid and mostly solid nodules demonstrating that these novel strategies have good results when compared with the radiologists segmentations, providing accurate pulmonary nodule volumes for posterior characterization and appropriate diagnosis.

1. Introduction and previous work

Lung cancer represents one of the main causes of death among all the possible diseases, being the leading cause of death among all the different cancers. As reference, the American Cancer Society estimated about 1.658.370 new cancer cases diagnosed and 589.430 cancer deaths in 2015, only in United States of America (American Cancer Society, 2015). From that estimation, 221.200 new cases and 158.040 deaths belong to lung cancer. For that reason, early detection and diagnosis becomes important in order to maximize the chances of survival of the patients, as happens with many other illnesses. From all the imaging modalities, Computerized Tomography (CT) is one of the most sensitive and adequate imaging technique to identify malignant nodules thanks to its image quality, resolution and level of detail, making CT clearly superior to any other modality, and widely used (as described by Van Ginneken (2008)). Over the years, Computer-Aided Diagnosis (CAD) systems have emerged in order to help the specialists in the lung cancer detection and diagnosis, facilitating their work. In general, the CAD systems try to identify malignant nodules inside the lung parenchyma using either chest radiography (Chen & Suzuki, 2013; Lee, Goo, Park, Lee, & Jin, 2012; Pereira, Fernandes, Mendonça, & Campilho, 2007) or CT imaging (Van Ginneken, 2008).

There is a large variability in CAD systems for lung cancer diagnosis that adopt different strategies, that can be organized in five consecutive main tasks: the lung parenchyma extraction, for segmenting the lung region; the lung nodule candidates detection, obtaining a group of structures that are suspicious of being a nodule; the refinement and final lung nodule detection, for reducing the number of false positives from the suspicious nodule candidates set; the segmentation of the nodule region, facilitating further local analysis; and the final benign/malignant differentiation. In this CAD scheme, the segmentation of the nodules is a crucial and complicated task aiming at providing the entire volume of the nodule,

* Corresponding author. Fax: +34981167160.
E-mail addresses: up201306966@fe.up.pt (L. Gonçalves), jnovo@udc.es (J. Novo), campilho@fe.up.pt (A. Campilho).

http://dx.doi.org/10.1016/j.eswa.2016.05.024
0957-4174/

which will be analyzed to determine its degree of malignancy. In that direction, if a good segmentation of the nodule is achieved, there is an increased probability of the degree of malignancy of a nodule be correctly evaluated. On the contrary, poor segmentations can lead to wrong nodule analysis and, therefore, poor evaluation.

Over the years, different methodologies were presented to segment lung nodules. In the different approaches we can find a large and heterogeneous set of possibilities. Most of the solutions start from previous detected regions, and then use different strategies for a detailed nodule segmentation. Many include thresholding, region growing, clustering or deformable models, sometimes combined with image pre-processing to facilitate the posterior lung nodule segmentation process. Here, a selected representative group of research approaches are presented to illustrate the state-of-the-art variability.

Some of the proposed methodologies, specially at the early days of CAD systems, used thresholding to obtain the nodule region. Hence, Armato, Giger, and MacMahon (2001) used multiple gray-level thresholds in the segmented lung parenchyma to extract individual structures. Then, an 18-point connectivity scheme is employed to group contiguous pixels in three-dimensional structures. These detections are further refined to obtain the final nodule segmentation. Kuhnigk et al. (2006) proposed an automatic segmentation method that employs a fixed threshold followed by morphological methods to extract the nodules. In the work of Messay, Hardie, and Rogers (2010) the proposal combines thresholding with morphological operators for segmentation. Setio, Jacobs, Gelderblom, and van Ginneken (2015) also designed a process where the nodule area is extracted using a multistage process including thresholding and morphological operations. Tuinstra (2008) designed a methodology that uses thresholding and morphological operators to perform an initial extraction combined with a regression system to obtain the final segmentation.

Many approaches use region growing techniques as part of the segmentation process. Zhao, Yankelevitz, Reeves, and Henschke (1999) proposed a method starting with a manually detected nodule and then decreasing progressively a high density threshold, working as a region growing technique, expanding the area of the nodule candidates step by step. This progressive region growing ends when consecutive thresholds provide either a diminished gradient strength in the detected boundary or if a shape compactness constraint is broken. Li, Li, and Doi (2008) also employed a region growing approach in a 3D segmentation process to extract the nodules. Kubota, Jerebko, Dewan, Salganicoff, and Krishnan (2011) implemented approaches that firstly distinguish radiographically denser anatomical structures from the rest of the lungs. Then, the identification of the core of the nodules with an Euclidean distance transform, combined with a region growing to separate the nodule from other attached structures. Finally, convex hull is computed to refine the final segmentation. Gu et al. (2013) uses a “click and grow” segmentation algorithm that basically starts from a seed selection by the user and a posterior process using region growing based on intensity similarity and proximity to areas with low intensity (air regions). The system uses multiple seeds and a posterior voting to determine the final segmentation.

Other approaches employed clustering methods to discriminate the lung nodule regions from the rest of the lung parenchyma or other structures like blood vessels. Nodule segmentation based on clustering was used by Antonelli, Frosini, Lazzerini, and Marcelloni (2005), where the authors automatically segmented the nodules using fuzzy C-means (FCM) followed by the morphological analysis of the remaining structures. FCM was also employed by Zhang, Zhang, Tang, and Wei (2012) where an improved version of the FCM is used in two steps: first, by detecting the centroids of the clusters and second, by nodule segmentation using the improved FCM. Approximations of deformable models to obtain a satisfactory lung nodule segmentation were also employed. Awad et al. (2012) employed a multi-parameter level set sparse field active surface (including edge, rolling, distribution or curvature, among others, as energy terms to be minimized) to progressively fit the nodule area. A Level set variation formulation was also included in the approach of Farag, El Munim, Graham, and Farag (2013) in a segmentation process, using no prior a circle shape to model, to model a lung nodule shape.

Machine learning approaches using Neural Networks were also used for nodule segmentation. Messay, Hardie, and Tuinstra (2015) proposed user assisted approaches using a Regression Neural Network (RNN), using a set of features computed for each nodule candidate. Zhao, Ji, Xia, and Zhang (2015) combined self-generating neural networks and particle swarm optimization (PSO) to segment the nodules and preserve the integrity in cavitary nodule segmentations.

Many other strategies were also used to face the problem. Badura and Pietka (2014) designed a two step process: firstly a fuzzy connectedness (FC) preliminary analysis, specially designed for nodules connected to pleura or vessels. Secondly, on these seed points evolutionary computation is used to shorten the FC analysis and improve the results. Zhao, Ma, Qiang, and Cui (2015) applied the split sample Davis-Putnam total least squares algorithm to optimize a rough initial segmentation with a posterior refinement. Rolling ball is also employed to ensure the extraction of lung nodules close to the pleura. Ye, Beddoe, and Slabaugh (2010) employed graph cuts to group super-pixels derived from a mean shift clustering defined in a 5D feature space. Chen et al. (2012) used a front surface propagation to discriminate the lung nodule region from the pulmonary blood vessels. Okada, Comaniciu, and Krishnan (2005) designed an ellipsoid model with an anisotropic Gaussian fitting, aiming for a robust model against margin-truncation induced by neighboring structures and variability. Okada et al. (2005) also proposed another semi-automatic approach based on the concept of the ellipsoid using a joint space-intensity likelihood ratio test to detect blob-like structures and was applied in this particular problem of lung tumor segmentation. Wang et al. (2009) implemented 3D extended dynamic programming models combined with a multidirection fusion technique to improve the final segmentation results. Wang (2007) proposed an approach that starts from the center of the volume of interest (VOI). A number of radial lines originating from the center of the VOI are used to obtain a projection image. Then, dynamic programming is used to detect the contour of the nodule, which is finally projected again in 3D to construct the final segmentation result.

Despite the fact that many methods were proposed, the automatic segmentation of lung nodule in CT scans is still considered a challenging issue as nodules present a large variability in shape, texture, intensity pattern and connectivity between nodules and anatomic structures as blood vessels or the pleural walls.

Hessian-based metrics are based on the principle of deriving the Hessian matrix, a matrix of second order partial derivatives, of the image and then calculating the eigenvalues. These eigenvalues are combined to enhance the target structures. These metrics have been very useful in many different applications, namely to detect tubular, blob or plate structures Yang and Cheng (2014), vessel segmentation in brain images, Tankyevych, Talbot, Dokládal, and Passat (2009), opthalmologic images Tsai, Lee, and Yu-Chih Chen (2015) or in ultrasound imaging Hennersperger et al. (2015).

Ersoy, Bunyak, Mackey, and Palaniappan (2008) analyzed the eigenvalues for cell detection in human cancer cell images. A multi-scale spot enhancement filter was designed by Shamekhi, Miran Baygi, Azarian, and Gooya (2015) to detect and isolate

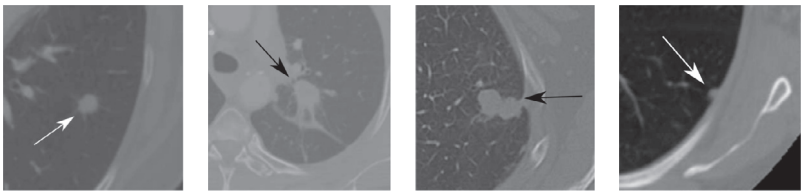

Fig. 1. (a) Well-circumscribed nodule. (b) Vascularized nodule. (c) Pleural-tail nodule. (d) Juxta-pleural nodule.

proteins in two dimensional gel electrophoresis images. Spots are also the target in the study of diabetic retinopathy in eye fundus images (Rubini & Kunthavai, 2015) using eigenvalues analysis to detect red dark spots in retinal images.

This work proposes new approaches for lung nodule segmentation using Hessian-based metrics. We started from the highly cited work of Murphy et al. (2009) that employs the Shape Index (SI) and Curvedness (CV) properties to extract the nodules. We adapted this single scale proposal to work as on multiple scales due to the large nodule size ranges that may appear in the lungs. Our approach uses the central medialness adaptive principle, originally proposed for tubular extraction (Krissian, Malandain, Ayache, Vaillant, & Trousset, 2000) and successfully applied in lung vessel segmentation Rudyanto et al. (2014). This approach was the winner of the VESSEL12 challenge. This motivated our application in nodule segmentation. We also propose the combination of both strategies, as the union of the detections provided by both approaches, with the aim of benefiting from the advantages of both.

This paper is organized as follows: Section 2 presents the chest CT image database that was employed to validate the proposed methods. Section 3 presents the different approaches for lung nodule segmentation. Section 4 shows the results, make comparisons with other approaches and with manual segmentations and discuss the results. Finally, Section 5 concludes this paper.

2. Materials

The materials used for development and validation in this research are a set of chest CT images from one of the most referenced public lung CT image databases, the Lung Image Database Consortium (LIDC) and Image Database Resource Initiative (IDRI) (Armato, 2011) database. LIDC-IDRI was initiated by the National Cancer Institute (NCI), afterwards continued by the Foundation for the National Institutes of Health (FNIH) along with the Food and Drug Administration (FDA) deriving in a large and complete lung cancer image database. The database contains thoracic CT scans as well as the diagnostic information with marked up and annotated lesions.

The LIDC-IDRI database contains 1.010 cases with 1.018 total scans, summing to a total of 243.958 images. Each CT scan includes an XML file that details several nodule information including lung nodule segmentations provided by four experienced thoracic radiologists. Each scan is characterized, using different features

Image characteristics The CT scans were imaged using different scanners and configurations. There are scans composed from 65 to 764 slices, corresponding to a wide range of slices and, therefore, slice spacing in z–direction. The x, y image resolution is 512×512 pixels.

Nodule position The database contains all types of nodules regarding their position in the lung parenchyma. There are juxta-pleural and pleural-tail nodules, juxta-vascular nodules and well-circumscribed nodules. Fig. 1a shows a well-circumscribed nodule located centrally in the lung without any connection to vasculature. An example of a juxta-vascular nodule is in Fig. 1b. It is in the center of the lung but connected to neighboring vessels. Fig. 1c presents a pleural-tail nodule, a designation due to a portion of the nodule being connected to the pleura surface by a thin tail. Finally, a juxta-pleural nodule is in Fig. 1d. This type of nodules have a large portion of the volume connected to the pleural surface.

Nodule size The majority of nodules has diameter greater than 3 mm. Nodule manual segmentations by specialists are provided. Regarding size, nodules with diameter ranging from 2.03 to 68.43 millimeters.

Nodule characteristics A large variability of nodule characteristics offered in the XML file including a set of properties like internal structure, subtlety, calcification, sphericity, margins definition, lobulation, spiculation, texture and degree of malignancy.

As indicated by the authors, (Armato, 2011), each scan was analyzed by a set of 4 experienced radiologists, who revised the scan to identify all the hypothetical nodules and characterized them using the above mentioned properties. In order to improve the quality of the annotations, this revision and annotation was performed in a two-step revision process: an initial blind revision and a second phase where each radiologist can check the analysis of the other three and confirm its own work.

The large size of the database or the large variability at image acquisition modes or the different nodule types offer adequate conditions for testing a methodology, as they cover several situations a CAD system could face in real scenarios. For that reason, the variability, the annotations and feedback provided by different specialists as well as being publicly available, placed this database as one of the most used in lung cancer study and research.

This database was used by different authors over the years in many problems regarding lung cancer diagnosis, namely, in lung segmentation (Novo, Rouco, Mendonça, & Campilho, 2014), nodule detection (Han et al., 2014; Jacobs et al., 2014; Saien, Hamid Pilevar, & Abrishami Moghaddam, 2015), nodule segmentation (Badura & Pietka, 2014; Diciotti, Lombardo, Falchini, Picozzi, & Mascalchi, 2011; Heckel et al., 2014; Sun et al., 2014), nodule characterization (Aggarwal, Vig, & Sardana, 2013; Han et al., 2013; Krewer et al., 2013) or specific issues like nodule's subtlety assessment (He, Sahiner, Gallas, Chen, & Petrick, 2014).

3. Methodology. Hessian-based approaches

An appropriate segmentation of the nodules is desired to maximize the potential of analysis and accurate discrimination between benign or malignant. In this paper we propose new approaches for lung nodule segmentation using Hessian-based strategies. We propose the use of the central adaptive medialness principle that we previously used in the lung nodule candidate detection task Novo, Gonçalves, Mendonça, and Campilho (2015) for nodule segmentation. We compare it with respect to an adapted version of another Hessian-based approach that was presented by

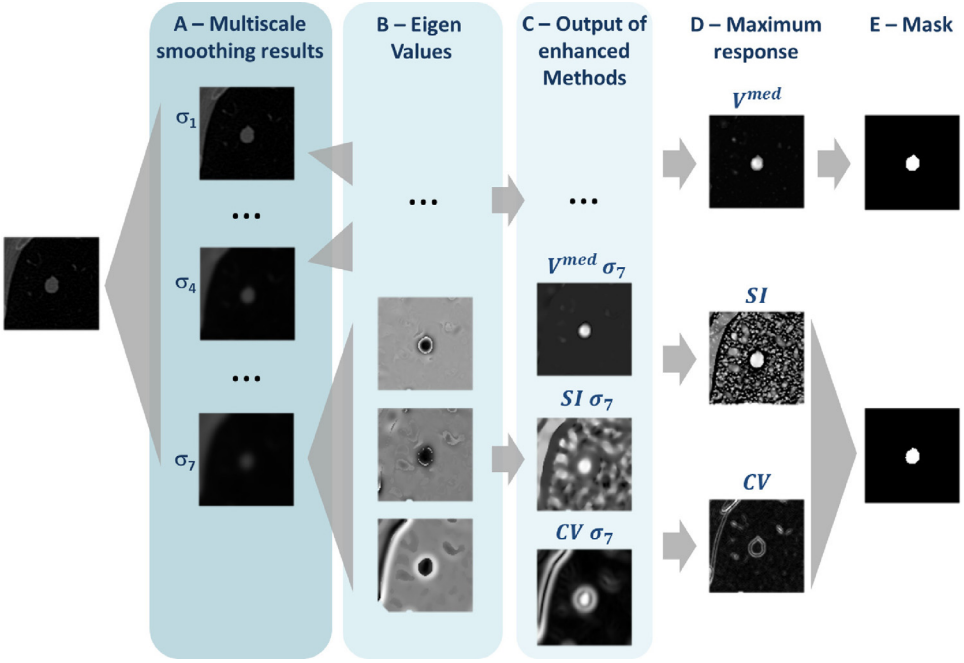

Fig. 2. Nodule segmentation scheme. A - Multiscale Gaussian smoothing using σ in the range 0.5 to 3.5, step 0.5. B - Eigenvalues computed from the Hessian Matrix. C - Nodule enhancement for each method for each σ. D - Maximum response. E - Final mask.

Murphy et al. (2009) for lung nodule identification and extraction, a well established method, frequently cited. The authors used the Shape Index (SI) and Curvedness (CV) properties to identify nodule candidates. Moreover, we formulate the combination of both strategies trying to take advantage of both strategies and compare it with respect to both of them, separately.

These strategies have an image enhancement step to obtain the 3D Hessian matrix at each voxel and calculate the corresponding eigenvalues. These eigenvalues are afterwards used to identify and segment lung nodules. We focus in the lung nodule segmentation and, therefore, assume that the approaches start from the location of a detected nodule in order to analyze and evaluate each proposal in the task of extraction the lung nodule volume. Fig. 2 presents the general scheme of the nodule segmentation process. Firstly, we use multiscale smoothing to reduce the level of noise and ease the nodule segmentation. After, the 3D Hessian matrix and the corresponding eigenvalues are computed and further combined by each method to finally generate the segmentation masks.

Given the considerable noise level that these CT scans present, a multiscale Gaussian smoothing filter G is applied over a range of σ's that corresponds to the sizes of the possible nodules. Thus, we remove noise and image artifacts as well as preserve the main structures of the nodules. Then, we have

$$L(I,\sigma) = I(p) * G(p,\sigma) \tag{1}$$

where $L(I, \sigma)$ is the result of the convolution between the image, I, and the Gaussian filter at a given σ and at a position p. An example of the multiscale Gaussian smoothing is illustrated in Fig. 2, stage A.

The Gaussian second order derivative of an image I with scale σ at a voxel x is defined by

$$\frac{\partial^2 I_\sigma}{\partial x^2} = I(x) * \frac{\partial^2 G(\sigma, x)}{\partial x^2} \tag{2}$$

Based on Eq. 2, the 3 × 3 Hessian matrix at a voxel $x = (x, y, z)$ for a given σ can be computed by

$$H(I)_\sigma = \begin{bmatrix} \frac{\partial^2 I_\sigma}{\partial x^2} & \frac{\partial^2 I_\sigma}{\partial x \partial y} & \frac{\partial^2 I_\sigma}{\partial x \partial z} \\ \frac{\partial^2 I_\sigma}{\partial y \partial x} & \frac{\partial^2 I_\sigma}{\partial y^2} & \frac{\partial^2 I_\sigma}{\partial y \partial z} \\ \frac{\partial^2 I_\sigma}{\partial z \partial x} & \frac{\partial^2 I_\sigma}{\partial z \partial y} & \frac{\partial^2 I_\sigma}{\partial z^2} \end{bmatrix} \tag{3}$$

Considering this Hessian matrix H for a given σ, three eigenvalues can be derived: $|\lambda_1| \leq |\lambda_2| \leq |\lambda_3|$ (shown in Fig. 2, stage B). These λ's are the basis of the structural detection strategies to enhance round structures, the nodular structures, as presented in Fig. 2, stage C.

As the chest CT scans include nodules with a large size variability, the response is defined over a range of σ's, each one enhancing the nodules of a given size. The final response is calculated as the combination of the responses from the considered scales. This combination is calculated as the maximum response for every voxel, as the following:

$$V^{med}(p) = \max_{\sigma_1 \leq \sigma_j \leq \sigma_n} V_{\sigma_j}(p) \tag{4}$$

where j is the scale of the σ and n the total number of σ's. Fig. 2, stage D illustrates the results obtained at this step.

Once we obtain the enhanced structures where the nodules can be clearly identified, the final step is a simple thresholding to select the voxels with a high response and, therefore, construct the masks by connectivity of the final nodule segmentations. The thresholds were empirically obtained by experimentation in a training set, in order to build a mask that would include, as accurate as possible, the region occupied by the nodule. An example of the output masks obtained by the different strategies can be seen in Fig. 2, stage E.

In the following subsections the different approaches are presented: one uses the central adaptive medialness; other is the Shape Index and Curvedness approach, and, finally, the combination of both strategies.

3.1. Shape index and curvedness approach

This strategy was originally proposed by Murphy et al. (2009), where the authors down-sample the image for efficiency and apply a single Gaussian filter ($\sigma = 1$). After obtaining the principal curvatures with $\sigma = 1$, the method derives SI and CV using the larger (λ_3) and the smaller (λ_1) eigenvalues of the Hessian matrix as follows:

$$SI = \frac{2}{\pi} arctan\left(\frac{\lambda_3 + \lambda_1}{\lambda_3 - \lambda_1}\right) \tag{5}$$

$$CV = \sqrt{\lambda_3^2 + \lambda_1^2} \tag{6}$$

Finally, the nodule segmentation masks are constructed by thresholding both SI and CV. The voxels that satisfy both criteria are considered as the final segmentations:

$$V^{SI-CV} = SI \cup CV \tag{7}$$

The main drawback of the original proposal was the application of a single σ. The method often detected parts of the nodule, as the selected scale may not fit to the nodule size, specially for large nodules. In this work, we adapted the strategy to overcome this drawback, by integrating the results over a range of σ's instead of a single one with the aim of guaranteeing that the entire nodule volume is identified.

3.2. Central adaptive medialness approach

The central adaptive medialness strategy is inspired by Krissian et al. (2000). This method uses λ_1, λ_2 and λ_3 as follows:

This method uses λ_1, λ_2 and λ_3 as follows:

$$V^{med}(\sigma, p)\begin{cases} 0 & \lambda_1 + \lambda_2 + \lambda_3 \geq 0 \\ -\frac{\lambda_2}{\lambda_3} \cdot (\lambda_2 + \lambda_3) & otherwise \end{cases} \tag{8}$$

In general terms, the method is only applied where the sum of the eigenvalues is less than 0, that is, for bright objects. In this case, we use the two largest eigenvalues to measure the structure strength, and their ratio is applied to correct the deviation from the center of the target structure.

This strategy has, as main advantage, a higher robustness with respect to noise. We previously applied this strategy in lung nodule candidate generation Novo et al. (2015), achieving good results. In this case, we adapt it to lung nodule segmentation to evaluate if it maintains the performance.

3.3. Combination of both Hessian-based approaches

Additionally, we combine both approaches, trying to explore the advantages of each method and aiming to replicate the segmentation as accurately as possible with respect to segmentations that are made manually by the specialists. The advantages of each strategy are:

- **SI and CV approach** – Sensible to small objects, details and to large intensity variations, therefore presenting high responses in the borders of the objects. It is more prone to noise enhancement, though.
- **Central adaptive medialness approach** – Can be object oriented, meaning that it can be tuned to enhance blob like structures and bypass other shapes as tubular shapes, corresponding to blood vessels, often source of errors.

The combination of both methods was implemented as the union of the detections that are provided by each approach. Thus, a voxel is included in a nodular region if it was detected by any of the strategies employed:

$$V^{comb} = V^{SI-CV} \cup V^{med} \tag{9}$$

Finally, a closing operation is applied to obtain the final segmentation mask. This step is done to smooth the boundaries of the mask and to obtain a more coherent nodule contour.

Table 1
Mean inter-observer Jaccard agreement index.

Nodules	Small	Medium	Big
Volume (mm^3)	< 500	$\geq$ 500-1000	> 1000
Mean	65.2%	71.6%	73.1%
St. deviation	9.3%	7.4%	9.2%

4. Results and discussion

In this section, different representative examples are presented to illustrate the capabilities of each method, including nodules with different characteristics. The accuracy of all the approaches is analyzed using the manual segmentations made by the radiologists.

The different approaches were validated using a total number of 569 solid and mostly solid nodules included in 700 images that were randomly selected from the LIDC-IDRI dataset, being 336 small, 90 medium and 143 large nodules. The size ranges were defined as in Table 1. This dataset was divided in training and test datasets, where the training dataset included the 10% of the nodules, 57, randomly picked from all of them. The rest of the nodules, 512, were used in the testing phases.

Only the nodules that were identified and characterized by all the four radiologists were taken. As mentioned in Section 2, we just analyzed those nodules that have a strong consensus among the four experienced radiologists that analyzed each scan.

No other restriction regarding image conditions or nodule characteristics were introduced in terms of subtlety, internal structure, calcification, sphericity, margin, lobulation, spiculation, texture and malignancy. Hence, our dataset contains a large nodule variability in terms of image characteristics and nodule conditions. The ROI has 100 voxel length in the x and y directions in order to accommodate the biggest sized nodule. For each particular nodule the length in the z direction has one additional voxel in the upper and lower limits of the nodule to be able to measure the intensity variation on this direction.

4.1. Parameter tuning

The different parameters of each approach were optimized on the training set with nodules randomly picked from all the 569 nodules. The rest of the nodules were employed in the validation process.

Regarding the image enhancement, we defined a range of σ's large enough to cover all the nodule sizes, corresponding to a range between 0.5 and 3.5, with increasing steps of 0.5. Thus, small nodules (about 3 mm) to large nodules (50 mm, 60 mm) can be identified and successfully segmented. Moreover, and as stated before, a multiscale Gaussian smoothing filter is applied over the range of σ's to remove possible noisy interferences and obtain better segmentations.

We used the following thresholds in the SI and CV adapted approach: $SI = 0.4$ and $CV = 0.005$. In the case of the central adaptive medialness approach, a threshold $V^{med} = 0.1$ was applied to identify the pixels that belong to the segmented nodules.

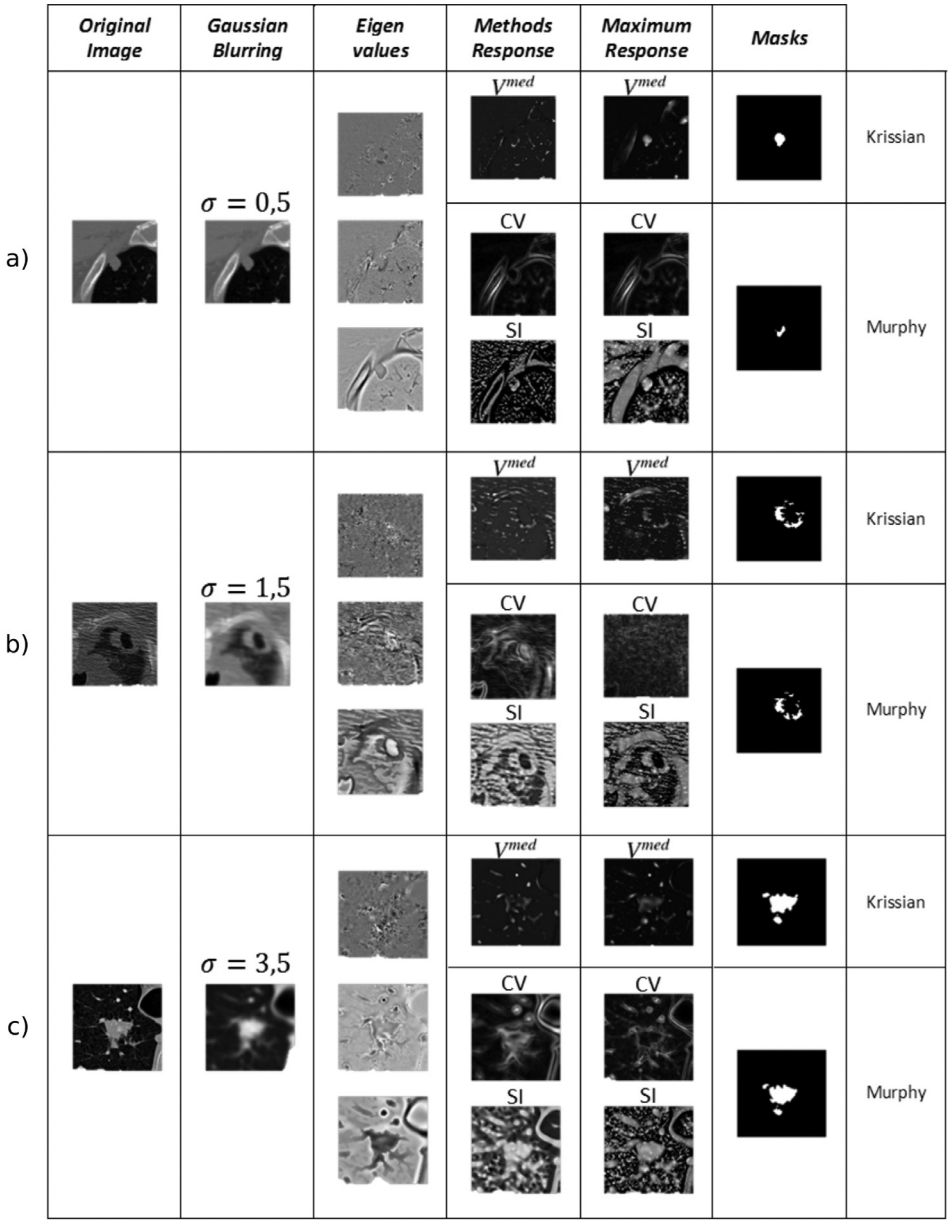

Fig. 3. All the stages of the segmentation process for a particular σ. Results for the central adaptive medialness and SI and CV strategies. The combination of both is the union of both masks: $V^{comb} = V^{SI-CV} \cup V^{med}$. The columns of Maximum Response and Masks give the result for all σ's. "Krissian" refers the central adaptive medialness strategy (Krissian et al., 2000). "Murphy" refers the CV and SI strategy (Murphy et al., 2009). (a) Stages for a medium, juxtapleural nodule, with a $\sigma = 0.5$. (b) Stages for a large, juxtapleural nodule, crossed by an airway (hole in black), with $\sigma = 1.5$. (c) Stages for a large, lobulated nodule, with $\sigma = 3.5$.

4.2. Nodule segmentation results

The methods were tested under a large variability of conditions, and the different approaches vary in the Hessian-based enhancement strategy. Fig. 3 shows the results obtained for different types of nodules, as two juxtapleural nodules and a lobulated one. Additionally, Fig. 3 shows the results for the SI and CV and central adaptive medialness strategies. The results of the combination of both methods correspond to the union of the final masks of both strategies: $V^{comb} = V^{SI-CV} \cup V^{med}$.

Fig. 3 also shows the partial results after each stage to illustrate the behaviour of all the components in the entire segmentation process. Although the process was performed in the entire 3D CT image, the results are illustrated with 2D representative slices only, in order to facilitate visualization. The first four columns show the input image, the image blurred with a Gaussian filter, the response of the three eigenvalues (λ_1, λ_2 and λ_3) of the Hessian matrix and each of the methods response (V^{med}, CV and SI) for a given σ, respectively. In each case, the results are presented with the most accurate σ for this particular nodule segmentation. The last columns show the maximum response over the range of σ's and the final mask obtained by each method.

Fig. 3a, presents the segmentation of a juxta-pleural nodule, with $\sigma = 0.5$. Juxta-pleural nodules are challenging situations as they are attached to the walls of the lungs and, in addition, they are smaller than many other nodules, making more difficult to locate the entire region that belongs to the nodule. It is visible that using the central adaptive medialness strategy a correct segmentation is obtained while the SI and CV adapted version does not. This is due to the fact that the SI and CV is particularly sensible to large intensity variations and has some difficulties in extracting structures close to spheres. Given that a pleural nodule has part of the

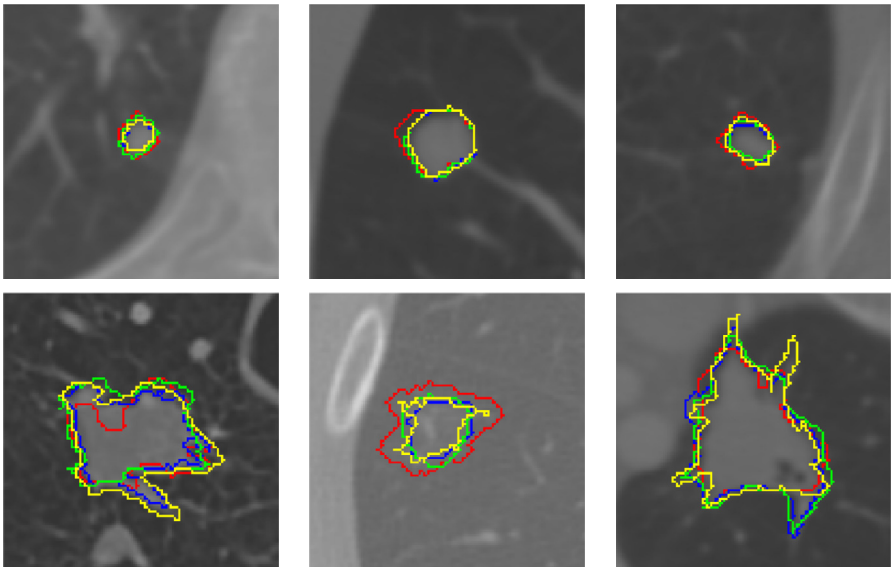

Fig. 4. Examples of nodule manual segmentations, represented by different colors, performed by radiologists in LIDC-IDRI image database. 1st row, simple nodules, easy to segment. 2nd row, irregular nodules, hard to segment.

body connected to the wall, and in this case, the variation occurs from the top left corner to the bottom right corner, the method enhances most of the lung and the nodule, although the far end of the nodule is brighter than the rest. When thresholding, only that brighter part is preserved instead of the entire nodule. The central adaptive medialness strategy can be tuned to enhance blob like structures with low response in the remaining lung, resulting in a good nodule segmentation.

Fig. 3b shows a difficult nodule segmentation situation, with $\sigma = 1.5$. It is a large juxtapleural nodule that is is placed in a complex location close to the pleura that also presents a very complex shape as it is crossed by an airway (the black hole that can be seen inside the nodule). Given that, the segmentations with both approaches are not as perfect as it would be desired. This is mainly due to the airway crossing its center, producing high positive eigenvalues resulting in a low response in V^{med}, CV and SI. Also, the fact that there is a connection between the nodule and the pleura makes it more difficult to detect roundness in this region.

The third one, Fig. 3c, presents the segmentation, using $\sigma = 3.5$, of a large and lobulated nodule, a very complex shape to be segmented. In general terms, the methods reaches the shape of the nodule, but failing to segment in the connection between the large portion of the nodule and its lobulated part. As in the previous case, lower intensities in this region produce a low response in the image enhancement step, being more complex to detect roundness in this particular region.

4.3. Agreement analysis between methods' segmentations and radiologists' segmentations

In order to analyze the similarity between the segmentations of the automatic approaches and the four radiologists, we have selected as mentioned only the nodules that were detected by all the four specialists.

In general, lung nodules with a continuous shape and obvious contour result in more similar segmentations made by the radiologists as the boundaries are clearly recognizable. On the contrary, lung nodules with complex shapes and irregular contours give rise to larger segmentation variability because their boundaries are not obvious. These different types of nodules, from easy to hard to segment, are presented in Fig. 4 to illustrate this situation. In particular, Fig. 4, 1st row shows three examples of solid nodules, with small or intermediate sizes with smooth and well defined contours. In this case, there is a good degree of agreement among the manual segmentations provided by the four specialists. On the contrary, Fig. 4, 2nd row, shows other three examples of nodules with complex shapes and irregular contours. In this other case, the radiologists have significant differences in their segmentations as it is not very clear where the limits of the nodules are. This disparity in their appreciation makes more complex the validation of the segmentation process.

The lung nodule segmentation approaches presented in this work have different performances in facing nodules with different levels of complexity. Thus, the results vary on the nodule size, their location, texture, definition or contour smoothness. Fig. 5 shows examples of segmentations with the proposed methods for different types of nodules. The most representative 2D slices are presented instead of the entire 3D nodule volume for a better visualization. In particular, four different results are shown: a big juxtavascular nodule, a big round and smooth juxtavascular nodule, a medium size juxtapleural nodule and a small size intraparenchymal nodule. Fig. 5a presents the ROIs where the nodules appear. Fig. 5b shows the outlines of the segmentations performed by both strategies: red line corresponds to the segmentation with the central adaptive medialness strategy whereas blue line corresponds to the SI and CV strategy.

Looking at these segmentations it is visible that the methods have different responses for nodules with different characteristics. In the case of Fig. 5b, 1st and 4th rows both methods have similar results so it is not clear which one performs the best. However, in the segmentation of the nodule in Fig. 5b, 2nd row, the SI and CV adapted approach clearly outperforms the central adaptive medialness method as the first approach tends to better perform when nodules are somehow round, well defined and purely intraparenchymal.

The opposite happens with the nodule of Fig. 5b, 3rd row where the central adaptive medialness method is capable to provide the entire nodule segmentation, whereas the SI and CV method only retrieves part of the nodule region. This happens because the SI and CV method pay special attention to the contour of structures with curvature. For that reason, this method has many

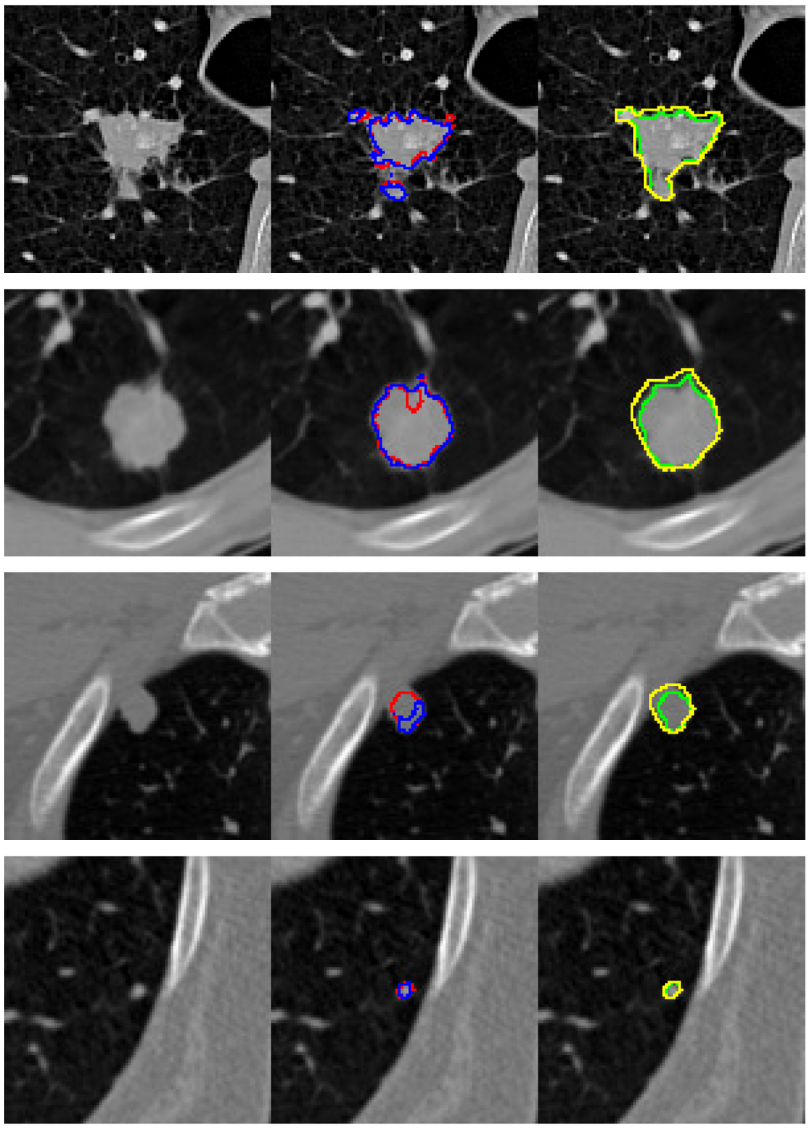

Fig. 5. Examples of segmentations for both methods, their combination and for the radiologists. (a) Original ROIs with nodules. (b) Outlines of the masks produced by both methods. The red line corresponds to the approach from central adaptive medialness and blue line to the SI and CV adapted approach. (c) Comparisons between the outlines of the final masks (green line) and the outlines of radiologists (yellow line). First row - A big, juxtavascular nodule. Second row - A big, round, juxtavascular nodule. Third row - Medium sized, juxtapleural nodule. Fourth row - A small, intra-parenchymal nodule. (For interpretation of the references to colour in this figure legend, the reader is referred to the web version of this article.)

problems in identifying the contour of nodular regions that are attached to the walls. That is what happens with the case of this juxtapleural nodule. On the contrary, the central adaptive medialness method can be tuned to enhance blob like structures, ignoring other lung parts, even when the objects are attached to the lung wall. In these situations, this method is capable of obtaining acceptable contours.

Here, the combination of both methods is also presented. In particular, Fig. 5c presents the combination of both strategies in green line and the comparison with respect to the radiologists segmentations, represented by a yellow line. The final segmentation provided by the specialists as the union of the manual segmentations from the four radiologists. As indicated, the segmentations of each approach are integrated in a single segmentation method, applying a final closing operation, which smooths the margins of the segmentation mask and corrects some poor segmentations as happens in the case of Fig. 5a, 1st row. From the results, it can be concluded that the combination provides more accurate results, joining the strengths of both approaches and obtaining better segmentations.

Moreover, considering the segmentation outlines that come from the combination of methods (green line) and the union of radiologists (yellow line) represented in Fig. 5c, it can be observed that the combination outperforms the radiologists segmentations. This happens as the specialists tend to mark the outline in a conservative way, guaranteeing that the entire nodule is enclosed in their segmentation. This derives in manual segmentations that tend to be outside of the nodule contour. The manual segmentation in the exact border would imply a more tedious and exhaustive work to be done in all the slices where the nodule is con-

tained. This drawback is overcome by the computational defined methods, as they are more accurate on the borders of the nodule.

4.3.1. Segmentation agreement

An agreement study was performed using the automatic segmentations and the manual segmentations of the radiologists in order to further evaluate the performance of the proposed approaches for lung nodule segmentation. As measure of agreement we used the Jaccard index for its simplicity and accurate representation of the agreement degree, often used to evaluate medical image segmentation tasks (Bouix et al., 2007; Lassen, Jacobs, Kuhnigk, van Ginneken, & van Rikxoort, 2015; Silva, Madeira, Santos, & Ferreira, 2011). Jaccard index was also selected as it is one of the most employed for lung segmentation evaluation.

To analyze of the segmentation agreement, we used as reference the degree of agreement between the four radiologists. This reference to evaluate the performance of the different approaches was studied in this work. Further comparisons were made using other state-of-the-art methods that used the same similarity measure and, moreover, that were validated on nodules from the LIDC-IDRI image dataset.

The Jaccard index is defined by:

$$Jaccard = \frac{A \cap B}{A \cup B} \tag{10}$$

where A and B represent the segmentations to be compared. The Jaccard index tends to one for a high level of agreement. In this case, with largely similar segmentations, their intersection is practically the same as the union. On the contrary, the Jaccard index tends to zero for a reduced level of agreement.

We evaluated the agreement of the segmentations between radiologists and the agreement of segmentations between the radiologists and each of the automatic methods and their combination. This resulted in three Jaccard values for each radiologist (each radiologist's segmentation is compared to the other three) and four Jaccard values for each one of the methods (one for a comparison with each radiologist's segmentation). By averaging the results, the mean value of agreement was derived for all radiologists and the mean value of agreement was derived for each of the methods and their combination. We used the average of the Jaccard index as the agreement measure due to the fact that the manual radiologists segmentations are anonymous. Consequently, it is impossible to link annotations of the same specialist over different cases. We average the indexes for each segmentation type so we can compare the agreement along the cases.

The inter expert agreement analysis results, depicted in Table 1, indicate a significant variability between the manual segmentations of the experts as the highest mean Jaccard value arises from segmentations of big nodules is 73%. This happens as often it is not easy to determine exactly the contour of the nodules, giving rise to significant discrepancies even between experienced radiologists. As visible in Table 1, the standard deviation in Jaccard measures varies from $\pm 7 - 10\%$, indicating that the agreement between observers in different nodules has a reasonable variation. These results show disagreements between radiologists even after a second labeling process with confirmation, which illustrates the level of complexity that a nodule segmentation approach has to face.

Table 2 includes the same analysis for each of the Hessian-based strategies and their combination. In general, the Hessian-based approaches have a performance within the levels of agreement between radiologists. However, there are representative differences among them. Although the SI and CV approach provides similar results to the performance of the radiologists, there are some cases where they are worse. On the other hand, the central medialness adaptive approach clearly outperforms the SI and CV statistics. it even improve the results that were obtained by the radiologists manual labeling, in all the nodule sizes. This means that this proposal not only provide adequate segmentation results but also includes a stable behaviour. Finally, the combination of both Hessian strategies offers the best results of all as it combines the accurate performance of both.

In medical imaging, the research community often have difficulties in the comparison with other approaches, as it is common the use of private image datasets or subsets of public image datasets without mentioning the cases that are selected, hampering the fair comparison among different approaches. There are different methods that were validated with LIDC images and used the same similarity index. Messay et al. (2015) includes a comparison of representative segmentation methods tested on nodules from the LIDC dataset indicating its similarity measurements thanks to the works of Wang (2007), Wang et al. (2009) and Kubota et al. (2011). The general idea of the included works are mainly introduced in Section 1. The results are summarized in Table 3. As we can see, these proposals have a large disparity in the similarity index. It should be noted that many of the approaches are semi-automatic, needing the inclusion of seed points or restrictions in the image to the nodule placement for a further segmentation process, as is faced in this work. Moreover, most of these approaches were analyzed with nodules with a majority of experts selection, that is, with the inclusion of at least 3 out of 4 radiologists. In our case, we considered the consensus among the four experts. Although all the approaches used nodules from the same image dataset, they were not exactly the same samples, therefore the results can vary given the large variability of the nodules in the dataset. Despite that differences, the comparison between the performance of our proposals, the performance of the state of the art approaches shown in Table 3, reinforce the idea that the new strategies can provide accurate results as many of the best methods of the literature.

Additionally, a further analysis was also made in the validation process. Considering that we have two different types of segmentations, from the automatic methods and from the radiologists, we employed in this analysis the Bland-Altman plot (Bland & Altman, 1999). This plot is identical as the Tukey mean-difference plot, but it was popularized in medical statistics by J.M. Bland and D.G. Altman, taking their names. The plot is used to measure the agreement between metrics of two different methods, comparing both metrics that are represented in a two-dimension plot. In our case, the metrics used are the Jaccard indexes previously calculated. In the Bland-Altman plots the vertical axis is the difference between the mean Jaccard value of the radiologists segmentations and the mean Jaccard value of the automatic methods (Mean Difference). The horizontal axis is their Mean Value.

We performed the Bland-Altman study dividing the nodules in size for the three methods. Figs. 6, 7 and 8 present the Bland-Altman plots for small, medium sized and big nodules, respectively. To divide the nodules by size we defined three ranges of sizes presented in Table 4.

Moreover, for better understanding, the global Mean Differences, and their standard deviation, for every Bland-Altman plots are presented in Table 4. Analyzing Table 4, it is visible that the central adaptive medialness method presents in general lower absolute values of the difference, indicating that it agrees more with the radiologists than the SI and CV does. The SI and CV adapted method, however, presents higher values indicating that the agreement is lower. This happens, as previously shown in Fig. 5, because sometimes the SI and CV adapted method fails in segmenting some cases, specially the ones attached to other lung structures. Moreover, the standard deviation is lower in the central medialness adaptive strategy, stating that this is a more stable proposal regarding the SI and CV approach.

The combination of both methods, however, present lower differences in all the cases, even better than the central adaptive

Table 2
Mean method vs radiologist Jaccard agreement index. SD, standard deviation. Murphy, SI and CV approach. Krissian, central adaptive medialness approach.

Nodule size	Murphy			Krissian			Combination		
	Mean	SD	Median	Mean	SD	Median	Mean	SD	Median
Small	61.4%	17.9%	66.8%	69.4%	7.8%	70.7%	69.7%	7.6%	71.0%
Medium	69.5%	13.3%	71.2%	73.1%	7.3%	73.8%	73.5%	6.4%	74.1%
Big	66.9%	14.9%	72.1%	73.0%	9.2%	75.3%	73.9%	8.7%	75.8%
Overall	64.1%	16.5%	68.8%	70.9%	8.1%	72.4%	71.3%	7.7%	72.7%

Table 3
Nodule segmentation performance comparison on LIDC nodules segmented among state of the art methods.* The system assumes a lung mask has been supplied and has limitation on the dimensions of the cropped VOI.** Second and third approaches are provided with multiple cues to the system to improve the results.

Method	Performance
Zhao et al. (1999), Wang et al. (2009)	43%
Okada and Akdemir (2005), Okada et al. (2005), Kubota et al. (2011)	45 ± 21%
Kuhnigk et al. (2006), Kubota et al. (2011)	56 ± 18%
Wang (2007)	64%
Tuinstra (2008)*	67% ± 16%
Li et al. (2008), Wang et al. (2009)	45%
Wang et al. (2009)	58%
Messay et al. (2010)	63 ± 16%
Kubota et al. (2011)	59 ± 19%
Messay et al. (2015)**	69.2 ± 13.8%
Messay et al. (2015)**	77.6 ± 8.6%
Messay et al. (2015)**	74.1 ± 9.9%

Table 4
Results for the Bland-Altman study. Mean of the difference between the mean Jaccard value of the radiologists and the mean Jaccard value of the methods segmentations. Murphy, SI and CV approach. Krissian, central adaptive medialness approach. SD, standard deviation of the differences.

Nodules	Murphy		Krissian		Combination	
	Mean	*SD*	*Mean*	*SD*	*Mean*	*SD*
Small	3.9%	18.9%	−4.1%	9.2%	−4.4%	8.8%
Medium	0.2%	11.8%	−1.5%	8.5%	−1.9%	8.3%
Big	6.2%	16.5%	0.1%	11.4%	−0.9%	10.9%

medialness approach alone, indicating that putting together both strategies shows a more reliable behaviour. This can be checked in Table 4, where the Bland-Altman values are more similar in all the cases, being specially better in the small nodules. This is probably the result of the lower agreement between radiologists for that size. In fact, the mean value tends to be lower as the nodules increase in size. Although this can seem surprising, small nodules have margins that are not well defined, so the segmentations can diverge greatly between observers. Due to their small size, small variations in the segmentation process can actually translate into segmentations that occupy a much bigger percentage of volume, resulting in a low agreement. On the other hand, big nodules are only difficult to outline when they are connected to vasculature and other structures. Even in those cases, the fact that the majority of their volume is clear, can lead all radiologists to equally outline most of the nodule. Moreover, the standard deviation is the lowest of all the approaches, confirming the tendency of a more stable method, improving also the results of the central medialness adaptive approach.

The Bland-Altman plots also show that the difference value between Jaccard values is farther from the Mean Difference when the Mean Values are lower for large and small nodules. In other words, the data is more scattered for lower Mean Values, which is the result of large variations between segmentations provided by radiologists for some nodules. This means that, because the radiologists do not agree with each other, then the agreement between them and the methods is, globally, also small. Although a segmentation obtained by the methods may be similar to one of the radiologists, it is probably different to the others.

We also analyzed if these differences are statistical significative. Table 5 includes the results of the t-test analysis over each of the methods and nodule sizes, with a significance level of 5%. As we can see, the lower performance of the SI and CV is significative in two of the three cases, deducing that this approach, although offer general acceptable results, does not reach the radiologists performance. However, the central medialness adaptive approach offers a statistical significative a better performance in small nodules, but being also quite close of the significance with medium nodules (p−value of 8%). In big nodules the performance is practically the same as the radiologists, concluding that this approach, in the worst cases offer a robust behaviour similar to the radiologists work, and in the best cases provide statistical significative correct segmentations. The combination, finally, outperforms the radiologists in all the cases, being statistical significative in two of the three cases (small and medium) but being quite close of the significance also with big nodules (p−value of 7%). This allow us to conclude, once again, that this proposal offers significative correct results, with a better performance than the individual strategies alone.

5. Conclusions

Given the large variability in image conditions and nodule characteristics, the lung nodule segmentation on chest CT scans is a crucial and challenging task that has to be faced by any CAD system, as a previous step to nodule characterization and lung cancer diagnosis. This paper present new approaches for lung nodule segmentation in chest CT images. These methods use and combine Hessian-based strategies that are defined deriving several parameters from the Hessian matrix and use them in different image enhancement strategies that identify the lung nodule regions and perform, therefore, the extraction of the nodules. The first proposal uses the principle of central adaptive medialness (Krissian et al., 2000). This strategy was originally formulated with the aim of detecting 3D tubular structures and that was applied satisfactorily in the task of vessel extraction in chest CT scans. This proposal was compared with another well established Hessian-based strategy, the SI and CV method (Murphy et al., 2009), one of the most popular and cited methods for lung nodule extraction. We adapted the SI and CV method to work as a multiscale method and segment nodules from a wide range of sizes. We previously used the central adaptive medialness principle in nodule candidate identification with satisfactory results, outperforming the results of the SI and CV method.

Additionally, we propose the combination of both strategies in a single approach with the aim of combining the advantages of both.

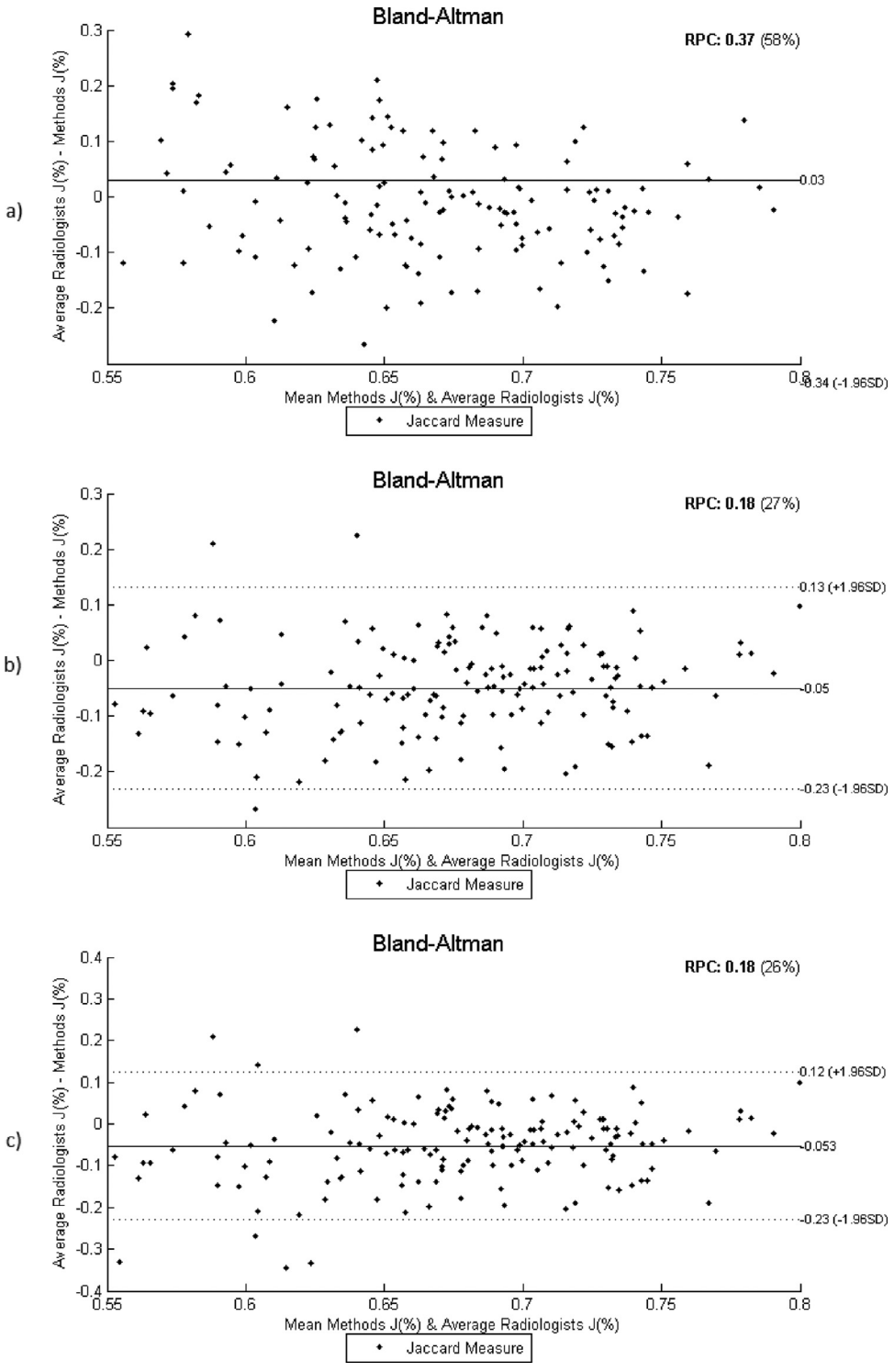

Fig. 6. Bland-Altman results for small nodules. RPC, reproducibility coefficient. RPC=1.96SD. SD, standard deviation. a) SI and CV adapted method. b) central adaptive medialness method. c) Combination of both.

Table 5
T-test statistical analysis of the Bland-Altman study at a significance level of 5%. Statistical significance of the differences and the associated $p-$values. Murphy, SI and CV approach. Krissian, central adaptive medialness approach.

Nodules	Murphy		Krissian		Combination	
	Significative	$p-$value	Significative	$p-$value	Significative	$p-$value
Small	Yes	$4.2363e^{-10}$	Yes	0.020936	Yes	0.0100
Medium	No	0.2762	No	0.0802	Yes	0.0061
Big	Yes	$2.9618e^{-4}$	No	0.9917	No	0.0739

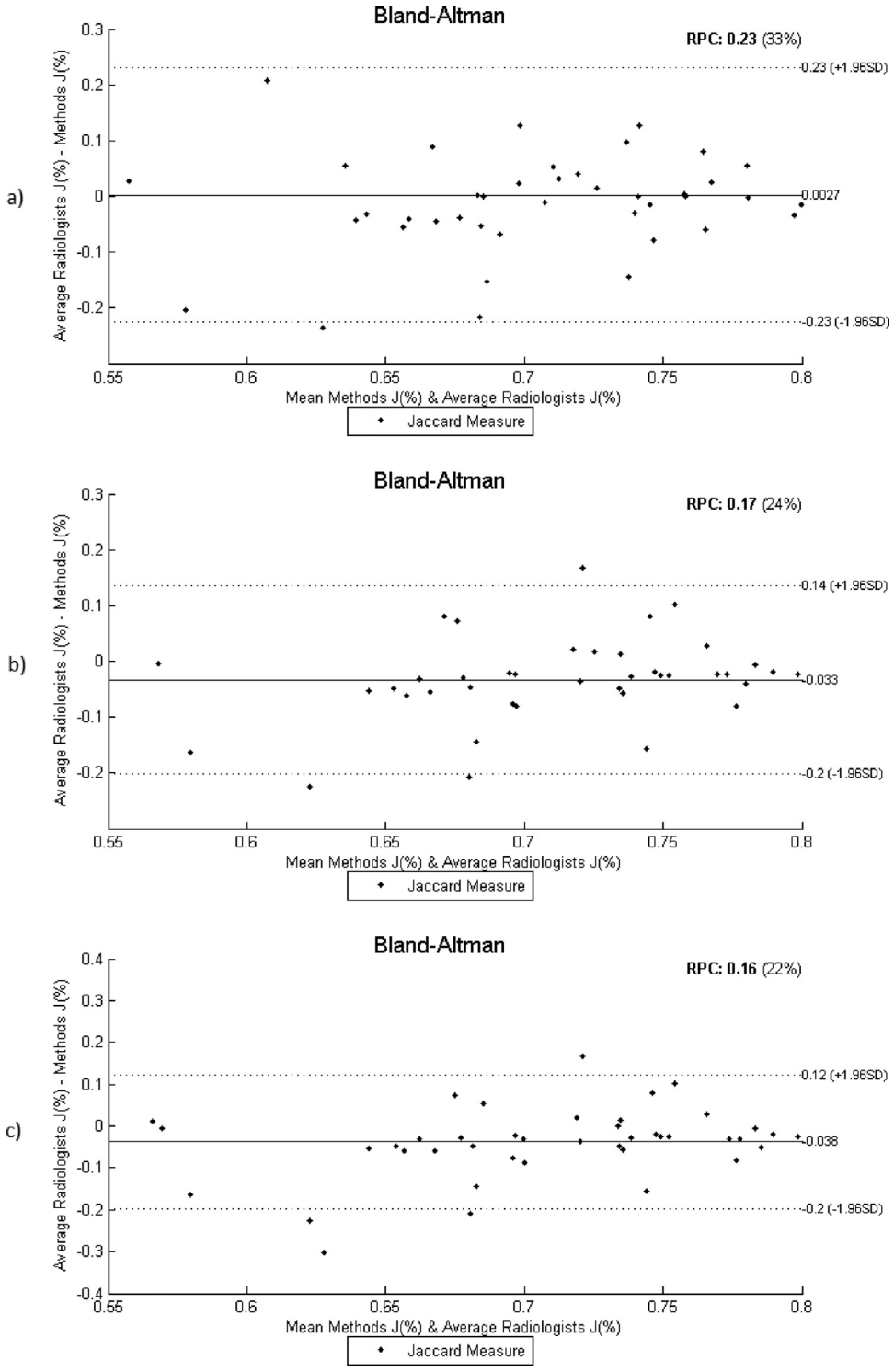

Fig. 7. Bland-Altman results for medium sized nodules. RPC, reproducibility coefficient. RPC=1.96SD. SD, standard deviation. (a) SI and CV adapted method. (b) central adaptive medialness method. (c) Combination of both.

The SI and CV method has as main advantages the sensibility to better enhance small objects, details and borders of the objects, whereas the central adaptive medialness method can be tuned to enhance blob like structures, ignoring other lung structures, even when the objects are attached to the lung wall. Thus, joining the segmentations of both approaches we obtained a more robust segmentation technique that provides results more similar to the radiologists.

We validated the methods with 569 solid and mostly solid nodules that present different characteristics. 10% of nodule dataset was used in the parameter tuning whereas the rest was used for validation. The results demonstrated that the central medialness adaptive approach provides accurate results. In general, this method presents nodule segmentations that are more similar to the manual segmentations of the specialists, outperforming the SI and CV method. However, the combination of both strategies

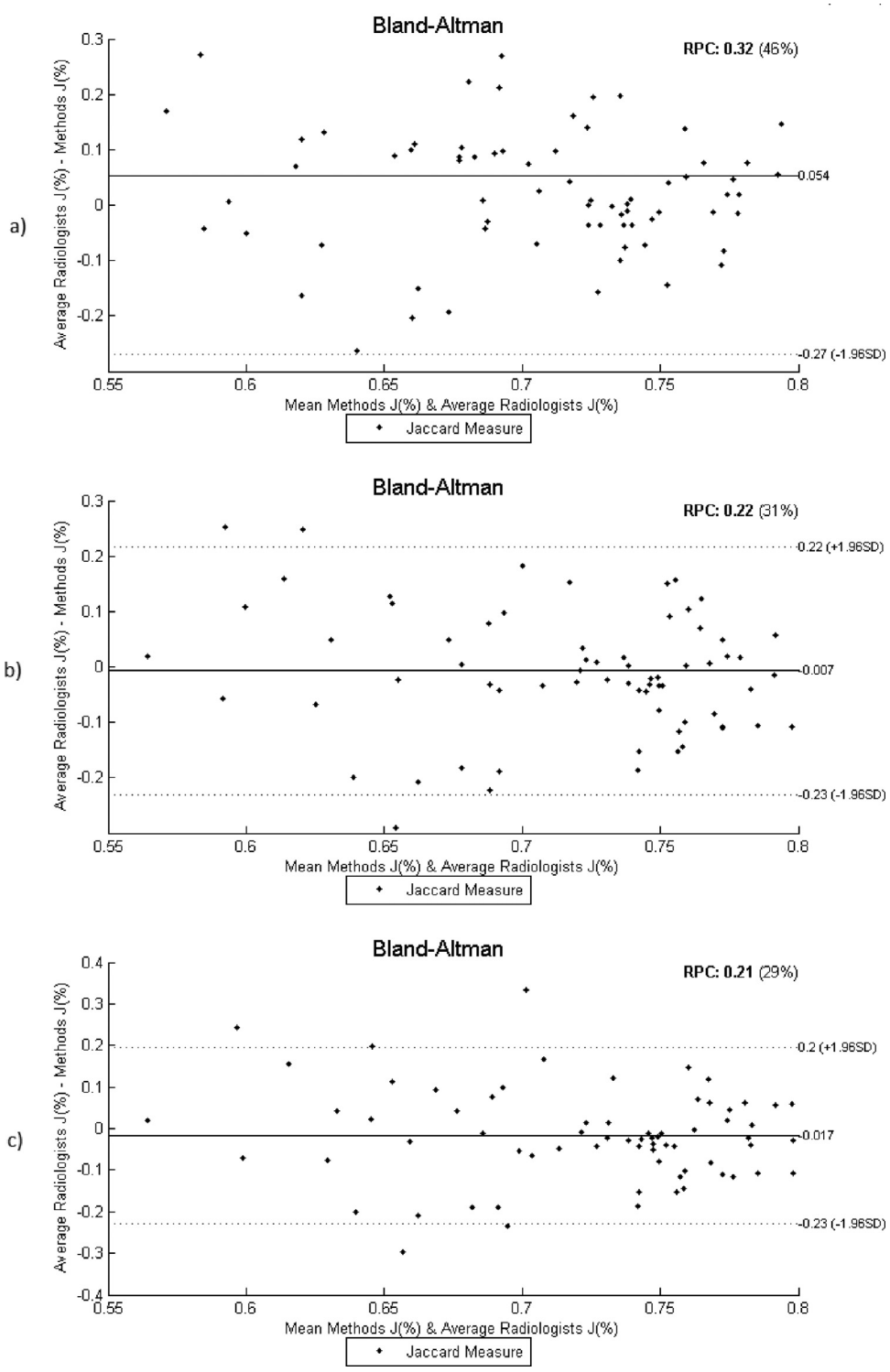

Fig. 8. Bland-Altman results for large nodules. RPC, reproducibility coefficient. RPC=1.96SD. SD, standard deviation. (a) SI and CV adapted method. (b) central adaptive medialness method. (c) Combination of both.

provided the best results in most of the cases, in comparison to both strategies alone.

Given the accuracy of these approaches for nodule candidate identification and lung nodule extraction, our next step will consist on the development of a nodule detection method, reducing the false positives that the Hessian strategies produce initially. We are also working in nodule analysis for benign/malignant classification. Hence, these nodule detection, segmentation and classification approaches can complete the entire CAD system for lung cancer analysis and diagnosis.

Acknowledgements

This work is financed by the ERDF – European Regional Development Fund through the Operational Programme for Competitiveness and Internationalisation – COMPETE 2020 Programme, and

by National Funds through the FCT – Fundação para a Ciência e a Tecnologia (Portuguese Foundation for Science and Technology) within project POCI-01-0145-FEDER-006961 and the grant contract SFRH/BPD/85663/2012 (J. Novo).

References

Aggarwal, P., Vig, R., & Sardana, H. (2013). Patient-wise versus nodule-wise classification of annotated pulmonary nodules using pathologically confirmed cases. *Journal of Computers (Finland), 8*(9), 2245–2255.

American Cancer Society (2015). *Cancer facts and figures*.

Antonelli, M., Frosini, G., Lazzerini, B., & Marcelloni, F. (2005). Automated detection of pulmonary nodules in ct scans. *International Conference on Computational Intelligence for Modelling, Control and Automation, 2*, 799–803.

Armato, S. G. (2011). The lung image database consortium (LIDC) and image database resource initiative (IDRI): a completed reference database of lung nodules on CT scans. *Medical Physics, 38*, 915–931.

Armato, S. G., Giger, M. L., & MacMahon, H. (2001). Automated detection of lung nodules in ct scans: Preliminary results. *Medical Physics, 28*(8), 1552–1561. http://dx.doi.org/10.1118/1.1387272.

Awad, J., Owrangi, A., Villemaire, L., O'Riordan, E., Parraga, G., & Fenster, A. (2012). Three-dimensional lung tumor segmentation from x-ray computed tomography using sparse field active models. *Medical Physics, 39*(2), 851–865.

Badura, P., & Pietka, E. (2014). Soft computing approach to 3D lung nodule segmentation in CT. *Computers in Biology and Medicine, 53*, 230–243.

Bland, J. M., & Altman, D. G. (1999). Measuring agreement in method comparison studies. *Statistical methods in medical research, 8*(2), 135–160.

Bouix, S., Martin-Fernandez, M., Ungar, L., Nakamura, M., Koo, M., McCarley, R., & ME, S. (2007). On evaluating brain tissue classifiers without a ground truth. *Neuroimage, 36*(4), 1207–1224.

Chen, B., Kitasaka, T., Honma, H., Takabatake, H., Mori, M., Natori, H., & Mori, K. (2012). Automatic segmentation of pulmonary blood vessels and nodules based on local intensity structure analysis and surface propagation in 3d chest ct images. *International Journal of Computer Assisted Radiology and Surgery, 2010*, 465–482.

Chen, S., & Suzuki, K. (2013). Computerized detection of lung nodules by means of 'virtual dual-energy' radiography. *IEEE Transactions on Biomedical Engineering, 60*(2), 369–378. doi:10.1109/TBME.2012.2226583.

Diciotti, S., Lombardo, S., Falchini, M., Picozzi, G., & Mascalchi, M. (2011). Automated segmentation refinement of small lung nodules in CT scans by local shape analysis. *IEEE Transactions on Biomedical Engineering, 58(12)*, 3418–3428.

Ersoy, I., Bunyak, F., Mackey, M., & Palaniappan, K. (2008). Cell segmentation using hessian-based detection and contour evolution with directional derivatives. *International Conference on Image Processing, ICIP'08*, 1804–1807.

Farag, A., El Munim, H., Graham, J., & Farag, A. (2013). A novel approach for lung nodules segmentation in chest ct using level sets. *IEEE Transactions on Image Processing, 22*(12), 5202–5213.

Gu, Y., Kumar, V., Hall, L. O., Goldgof, D. B., Li, C.-Y., Korn, R., … Gillies, R. J. (2013). Automated delineation of lung tumors from {CT} images using a single click ensemble segmentation approach. *Pattern Recognition, 46*(3), 692–702.

Han, F., Wang, H., Song, B., Zhang, G., Lu, H., Moore, W., … Liang, Z. (2013). A new 3d texture feature based computer-aided diagnosis approach to differentiate pulmonary nodules. In *Proceedings of spie - the international society for optical engineering. (vol. 8670)*.

Han, H., Li, L., Wang, H., Zhang, H., Moore, W., & Liang, Z. (2014). A novel computer-aided detection system for pulmonary nodule identification in ct images. *Progress in biomedical optics and imaging - proceedings of spie. (vol. 9035)*.

He, X., Sahiner, B., Gallas, B., Chen, W., & Petrick, N. (2014). Computerized characterization of lung nodule subtlety using thoracic ct images. *Physics in Medicine and Biology*, (4), 897–910.

Heckel, F., Meine, H., Moltz, J., Kuhnigk, J., Heverhagen, J., Kiessling, A., … Hahn, H. (2014). Segmentation-based partial volume correction for volume estimation of solid lesions in CT. *IEEE Transactions on Medical Imaging, 33(2)*, 462–480.

Hennersperger, C., Baust, M., Waelkens, P., Karamalis, A., Ahmadi, S., & Navab, N. (2015). Multi-scale tubular structure detection in ultrasound imaging. *IEEE Transactions on Medical Imaging, 34*(1), 13–26.

Jacobs, C., van Rikxoort, E., Twellmann, T., Scholten, E., de Jong, P., Kuhnigk, J.-M., … van Ginneken, B. (2014). Automatic detection of subsolid pulmonary nodules in thoracic computed tomography images. *Medical Image Analysis, 18*(2), 374–384.

Krewer, H., Geiger, B., Hall, L., Goldgof, D., Gu, Y., Tockman, M., & Gillies, R. (2013). Effect of texture features in computer aided diagnosis of pulmonary nodules in low-dose computed tomography. In *Proceedings - 2013 ieee international conference on systems, man, and cybernetics, smc 2013* (pp. 3887–3891).

Krissian, K., Malandain, G., Ayache, N., Vaillant, R., & Trousset, Y. (2000). Model-based detection of tubular structures in 3d images. *Computer vision and image understanding, 80*(2), 130–171.

Kubota, T., Jerebko, A., Dewan, M., Salganicoff, M., & Krishnan, A. (2011). Segmentation of pulmonary nodules of various densities with morphological approaches and convexity models. *Medical Image Analysis, 15*, 133–154.

Kuhnigk, J., Dicken, V., Bornemann, L., Bakai, A., Wormanns, D., Krass, S., & Peitgen, H. (2006). Morphological segmentation and partial volume analysis for volumetry of solid pulmonary lesions in thoracic CT scans. *IEEE Transactions on Medical Imaging, 25*, 417–434.

Lassen, B., Jacobs, C., Kuhnigk, J., van Ginneken, B., & van Rikxoort, E. (2015). Robust semi-automatic segmentation of pulmonary subsolid nodules in chest computed tomography scans. *Physics in medicine and biology, 60*(3), 1307–1323.

Lee, K., Goo, J., Park, C., Lee, H., & Jin, K. (2012). Computer-aided detection of malignant lung nodules on chest radiographs: Effect on observers' performance. *Korean Journal of Radiology, 13*(5), 564–571. doi:10.3348/kjr.2012.13.5.564.

Li, Q., Li, F., & Doi, K. (2008). Computerized detection of lung nodules in thin-section CT images by use of selective enhancement filters and an automated rule-based classifier. *Academic Radiology, 15*, 165–175.

Messay, T., Hardie, R., & Rogers, S. (2010). A new computationally efficient CAD system for pulmonary nodule detection in CT imagery. *Medical Image Analysis, 14*, 390–406.

Messay, T., Hardie, R., & Tuinstra, T. (2015). Segmentation of pulmonary nodules in computed tomography using a regression neural network approach and its application to the lung image database consortium and image database resource initiative dataset. *Medical Image Analysis, 22*(1), 48–62.

Murphy, K., van Ginneken, B., Schilham, A., de Hoop, B., Gietema, H., & Prokop, M. (2009). A large-scale evaluation of automatic pulmonary nodule detection in chest ct using local image features and k-nearest-neighbour classification. *Elsevier-Medical Image Analysis, 13*, 757–770.

Novo, J., Gonçalves, L., Mendonça, A. M., & Campilho, A. (2015). 3d lung nodule candidates detection in multiple scales. In *Mva 2015-iapr international conference on machine vision applications* (pp. 5–8).

Novo, J., Rouco, J., Mendonça, A., & Campilho, A. (2014). Reliable lung segmentation methodology by including juxtapleural nodules, *8815*, 227–235.

Okada, K., & Akdemir, U. (2005). Blob segmentation using joint space-intensity likelihood ratio test: application to 3D tumor segmentation. *IEEE Computer Society Conference on Computer Vision and Pattern Recognition, CVPR'05*, 437–444.

Okada, K., Comaniciu, D., & Krishnan, A. (2005). Robust anisotropic gaussian fitting for volumetric characterization of pulmonary nodules in multislice CT. *IEEE Transactions on Medical Imaging, 24*, 409–423.

Pereira, C., Fernandes, H., Mendonça, A., & Campilho, A. (2007). Detection of lung nodule candidates in chest radiographs. *Pattern recognition and image analysis, third iberian conference, ibpria 2007*.

Rubini, S., & Kunthavai, A. (2015). Diabetic retinopathy detection based on eigenvalues of the hessian matrix. *Procedia Computer Science, 47*, 311–318.

Rudyanto, R. D., Kerkstra, S., van Rikxoort, E. M., Fetita, C., Brilletc, P. Y., & Lefevre, C. (2014). Comparing algorithms for automated vessel segmentation in computed tomography scans of the lung: the {VESSEL12} study. *Medical Image Analysis, 18*(7), 1217–1232.

Saien, S., Hamid Pilevar, A., & Abrishami Moghaddam, H. (2015). Refinement of lung nodule candidates based on local geometric shape analysis and laplacian of gaussian kernels. *Computers in Biology and Medicine, 54*, 188–198.

Setio, A., Jacobs, C., Gelderblom, J., & van Ginneken, B. (2015). Automatic detection of large pulmonary solid nodules in thoracic ct images. *Medical Physics, 42*(10), 5642–5653.

Shamekhi, S., Miran Baygi, M., Azarian, B., & Gooya, A. (2015). A novel multi-scale hessian based spot enhancement filter for two dimensional gel electrophoresis images. *Computers in Biology Medicine, 66*, 154–169.

Silva, S., Madeira, J., Santos, B. S., & Ferreira, C. (2011). Inter-observer variability assessment of a left ventricle segmentation tool applied to 4d mdct images of the heart. In *Engineering in medicine and biology society, embc, 2011 annual international conference of the ieee* (pp. 3411–3414). IEEE.

Sun, S., Guo, Y., Guan, Y., Ren, H., Fan, L., & Kang, Y. (2014). Juxta-vascular nodule segmentation based on flow entropy and geodesic distance. *IEEE Journal of Biomedical and Health Informatics, 18(4)*, 1355–1362.

Tankyevych, O., Talbot, H., Dokládal, P., & Passat, N. (2009). Direction-adaptive grey-level morphology. application to 3D vascular brain imaging. *International Conference on Image Processing, ICIP'09*, 2261–2264.

Tsai, Y., Lee, H., & Yu-Chih Chen, M. (2015). Automatic segmentation of vessels from angiogram sequences using adaptive feature transformation. *Computers in Biology Medicine, 62*, 239–253.

Tuinstra, T. (2008). *Automatic segmentation of small pulmonary nodules in computed tomography data using a radial basis function neural network with application to volume estimation*. University of Dayton. Ph.D. Thesis.

Van Ginneken, B. (2008). Computer-aided diagnosis in thoracic computed tomography. *Imaging Decisions MRI, 12*(3), 11–22. doi:10.1111/j.1617-0830.2009.00129.x.

Wang, E. R. L. Q. J. (2007). Segmentation of pulmonary nodules in three-dimensional CT images by use of a spiral-scanning technique. *Medical Physics, 34*, 4678–4689.

Wang, Q., Song, E., Jin, R., Han, P., Wang, X., Zhou, Y., & Zeng, J. (2009). Segmentation of lung nodules in computed tomography images using dynamic programming and multidirection fusion techniques. *Academic Radiology, 16*, 678–688.

Yang, S., & Cheng, C. (2014). Fast computation of hessian-based enhancement filters for medical images. *Computer Methods and Programs Biomedicine, 116*(3), 215–225.

Ye, X., Beddoe, G., & Slabaugh, G. (2010). Automcatic graph cut segmentation of lesions in ct using mean shift superpixels. *International Journal of Biomedical Imaging, 2010*, 1–14.

Zhang, X., Zhang, C., Tang, W., & Wei, Z. (2012). Medical image segmentation using improved fcm. *Science China Information Sciences, 55*(5), 1052–1061.

Zhao, B., Yankelevitz, D., Reeves, A., & Henschke, C. (1999). Two-dimensional multi-criterion segmentation of pulmonary nodules on helical ct images. *Medical Physics, 26*(6), 889–895. http://dx.doi.org/10.1118/1.598605.

Zhao, J., Ji, G., Xia, Y., & Zhang, X. (2015). Cavitary nodule segmentation in computed tomography images based on self-generating neural networks and particle swarm optimisation. *International Journal of Bio-Inspired Computation, 7*(1), 62–67.

Zhao, J., Ma, R., Qiang, Y., & Cui, Z. (2015). Solitary pulmonary nodule segmentation based on the rolling ball method. *Journal of Computational and Theoretical Nanoscience, 12*(8), 1977–1983.